URSI GASS 2021,Rome, Italy,28 August- 4 September 2021

Microwave Sparse Imaging Applied to Stroke Monitoring

Marija Nikolic Stevanovic[(1)], Tushar Singh [(1),(2)], Branislav Ninkovic[(2)], and Branko Kolundzija [(1)(2)]
(1) School of Electrical Engineering, University of Belgrade, 11000 Belgrade, Serbia, www.etf.rs
(2) WIPL, Belgrade, Serbia, www.wipl-d.com

Abstract

We study the application of differential microwave sparse imaging in brain diagnostics. In particular, we describe the estimation stroke change between the consecutive measurements using l_1 regularization. The method is verified using a realistic anthropomorphic human phantom.

1 Introduction

Medical microwave imaging (MMWI) has recently gained its popularity due to the utilization of non-ionizing radiation and affordable components [1], [2]. At present, the golden standards in medical diagnostics are magnetic resonance imaging (MRI) and X-ray computerized tomography (CT), which provide high-resolution images. However, such systems are expensive and non-portable, which are significant drawbacks in many applications, such as patient bedside monitoring.

Among many potential MMWI applications, microwave brain imaging seems the most promising [3]-[5] due to a significant permittivity contrast between the healthy and stroke tissues [1]. In particular, the research and medical community are interested in tracking the stroke evolution over the course of time. Since the stroke changes slowly between the measurements, the reconstruction problem can be formulated using the linearized inverse scattering equation. Appropriate algorithms are truncated singular value decomposition (TSVD) [6], linear sampling method (LSM) [7], sparse processing [8]-[12], and many others. However, in the cases when the target (e.g., stroke variation) occupies a fraction of the search space, the sparse processing or l_1 regularization is particularly suitable.

The sparse processing has been widely used in solving inverse electromagnetic problems [8]. Some examples are: complex shape estimation [9], [10], medical diagnostics [11], [12], through-the-wall imaging [13], etc. Initial results were presented in [12], were vertically polarized infinitesimally small dipoles served as the sensors. Here, we consider a realistic measurement system composed of patch antennas placed above an anthropomorphic human phantom [14].

The paper is organized as follows. After the Introduction, in Section II we describe the numerical model and the sparse processing algorithm. In Section III we describe the numerical phantom. Section IV presents the numerical results. Finally, in the conclusion, we discuss the obtained results and give guidelines for future work.

2 Numerical Model

We consider a measurement system, consisting of M antennas, located in an inhomogeneous linear medium, of known permittivity ε_b. The measurement system is used for detecting a target of unknown permittivity ε. Fig. 1 shows an example of such system consisting of a target (depicted as a yellow ellipse) and two antennas, whose locations are given by the position vectors $\mathbf{r}_1$ and $\mathbf{r}_2$.

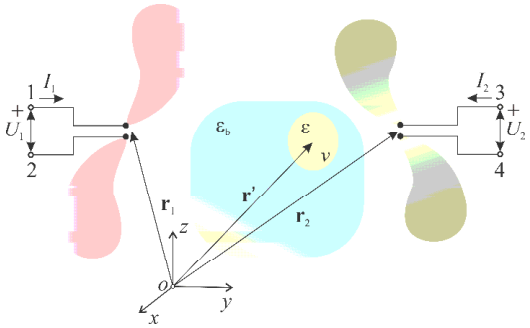

Figure 1. Example of the measurement system and a target located in a nonhomogeneous background medium.

From the scattering equation, it follows that the transmission between the antennas is [15]

$$\Delta s_{ij} \propto \int_{v'} (\varepsilon(\mathbf{r}') - \varepsilon_b(\mathbf{r}'))\mathbf{E}_{\text{inc}}(\mathbf{r}';\mathbf{r}_i)\cdot\mathbf{E}_{\text{tot}}(\mathbf{r}';\mathbf{r}_j)\,dv', \quad (1)$$

$$\Delta s_{ij} = s_{ij} - s_{ij}^0,$$

where s_{ij} and s_{ij}^0 are the transmission coefficients calculated when the target is present and absent, respectively; $\mathbf{r}_i$ is the location of receiving antenna; $\mathbf{r}_j$ is the location of the transmitting antenna; $\mathbf{r}'$ is the location of a point inside the target; $\mathbf{E}_{\text{inc}}(\mathbf{r}';\mathbf{r}_i)$ is the incident electric field at $\mathbf{r}'$ produced by the ith antenna when operating as the transmitter; and $\mathbf{E}_{\text{tot}}(\mathbf{r}';\mathbf{r}_j)$ is the total electric field at $\mathbf{r}'$ produced by the jth antenna. If the target is electrically small Born approximation is used, i.e., $\mathbf{E}_{\text{tot}} \approx \mathbf{E}_{\text{inc}}$. Hence, the transfer between the antennas becomes

$$\Delta s_{ij} \propto \int_{v'} \Delta\varepsilon(\mathbf{r}')\mathbf{E}_{\text{inc}}(\mathbf{r}',\mathbf{r}_i)\cdot\mathbf{E}_{\text{inc}}(\mathbf{r}',\mathbf{r}_j)\,dv', \quad (2)$$

$$\Delta\varepsilon(\mathbf{r}') = \varepsilon(\mathbf{r}') - \varepsilon_b(\mathbf{r}') \ . \tag{3}$$

In order to numerically implement the scattering equation, we discretize the search space into a uniform three-dimensional (3D) grid. In the discrete case, (2) becomes

$$\Delta s_{ij} \propto \sum_{i=1}^{L} \Delta\varepsilon_l \mathbf{E}_{\text{inc}}(\mathbf{q}_l, \mathbf{r}_i) \cdot \mathbf{E}_{\text{inc}}(\mathbf{q}_l, \mathbf{r}_j), \tag{4}$$

where $\mathbf{q}_l$ is the position vector of the l-th voxel, $\Delta\varepsilon_l$ is the correposnding permittivity difference, $l = 1, \ldots, L$, and L is the total number of voxels. In the matrix form, we have

$$\Delta\mathbf{s} = \mathbf{L}\Delta\boldsymbol{\varepsilon}, \tag{5}$$

$$\Delta\mathbf{s} = \begin{bmatrix} \Delta s_{1,1} & \cdots & \Delta s_{M,M} \end{bmatrix}^{\mathrm{T}} \tag{6}$$

$$\Delta\boldsymbol{\varepsilon} = \begin{bmatrix} \Delta\varepsilon_1 & \cdots & \Delta\varepsilon_L \end{bmatrix}^{\mathrm{T}}, \tag{7}$$

$$\mathbf{L} = \begin{bmatrix} \underline{\mathbf{E}}_{\text{inc}}(\mathbf{q}_1, \mathbf{r}_1) \cdot \underline{\mathbf{E}}_{\text{inc}}(\mathbf{q}_1, \mathbf{r}_1) & \cdots & \underline{\mathbf{E}}_{\text{inc}}(\mathbf{q}_L, \mathbf{r}_1) \cdot \underline{\mathbf{E}}_{\text{inc}}(\mathbf{q}_L, \mathbf{r}_1) \\ \vdots & \ddots & \vdots \\ \underline{\mathbf{E}}_{\text{inc}}(\mathbf{q}_1, \mathbf{r}_M) \cdot \underline{\mathbf{E}}_{\text{inc}}(\mathbf{q}_1, \mathbf{r}_M) & \cdots & \underline{\mathbf{E}}_{\text{inc}}(\mathbf{q}_L, \mathbf{r}_M) \cdot \underline{\mathbf{E}}_{\text{inc}}(\mathbf{q}_L, \mathbf{r}_M) \end{bmatrix}. \tag{8}$$

In order to solve (5), the sparsity constraint is applied. Hence, the minimization function is

$$\Delta\hat{\boldsymbol{\varepsilon}} = \min_{\Delta\boldsymbol{\varepsilon}} \left\{ \left\| \Delta\mathbf{s} - \mathbf{L}\Delta\boldsymbol{\varepsilon} \right\|_2^2 + \lambda \left\| \Delta\boldsymbol{\varepsilon} \right\|_1 \right\}, \tag{9}$$

where the coefficient λ balances between the mean-square error and the l_1 norm of the solution vector.

3 Numerical Phantom

To verify the algorithm, we used a numerical model of an anthropomorphic human phantom designed for the testing of microwave imaging systems [14]. The physical phantom [14] was produced by means of additive manufacturing (3D printing). The phantom consisted of several parts, all made of acrylonitrile butadiene styrene (ABS), which were clipped and glued together.

The numerical phantom was obtained by converting the STL triangular mesh into a quadrilateral mesh suitable for method of moments analysis [16], [17]. The model consists of 5 homogeneous domains, whose outer boundaries are shown in Fig. 2(a)-(e).The domains are: 3 mm thick head cavity, head mimicking tissue, 3 mm thick brain cavity, brain mimicking tissue, and a stroke. The head and brain cavity are assumed to be made of ABS. For simplicity, the head and brain mimicking tissues have the same properties, which were obtained by averaging the electromagnetic parameters of the white and grey matter [14]. The stroke was modeled as a spherical inclusion whose electromagnetic parameters were the same as those of blood. The permittivity and conductivity of all domains related to the phantom at $f = 1\,\text{GHz}$ are given in Tab. 1.

The microwave imaging system, depicted in Fig. 2(d), consists of 24 microstrip patch antennas, whose design and positioning were inspired by the antenna array used in [6].

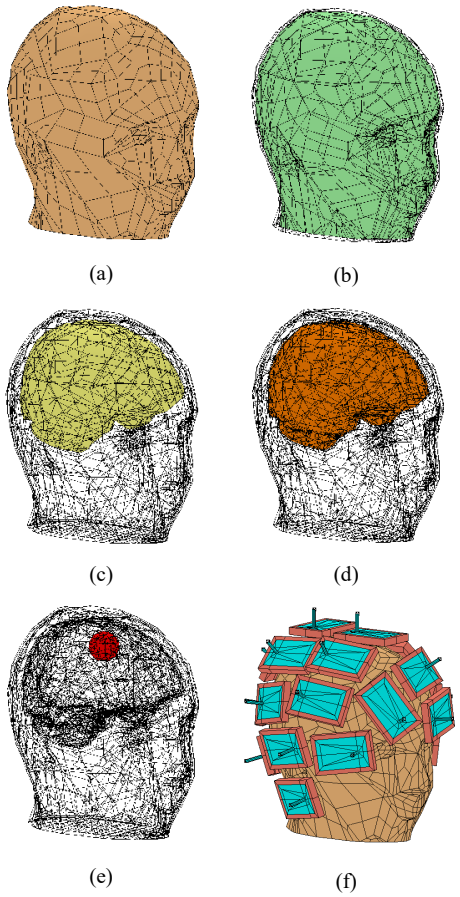

Figure 2. Numerical phantom. Outer boundaries of (a) the head phantom made of 3 mm thick ABS layer, (b) head mimicking tissue, (c) 3 mm thick brain layer made of ABS, and (d) the stroke. (e) The antenna array and the phantom.

Table 2. Permittivity and conductivity of the materials used in numerical phantom depicted in Fig. 1 at $f = 1\,\text{GHz}$.

Material	**Permittivity** ε_r	**Conductivity** $\sigma\,[\text{S/m}]$
ABS	3	0.004
Brain	45.388609	0.77302
Head	45.388609	0.77302
Stroke (Blood)	63.414607	1.576326

4 Numerical Results

The electromagnetic analysis of the microwave imaging scenario shown in Fig. 1 was performed using WIPL-D Pro software [16]. To compute the differential scattering parameters, the simulations with and without the stroke were needed. The incident electric field was computed using the model without the stroke at 7 cuts parallel to the $x0y$ plane. In each cut, there were 50×50 field points.

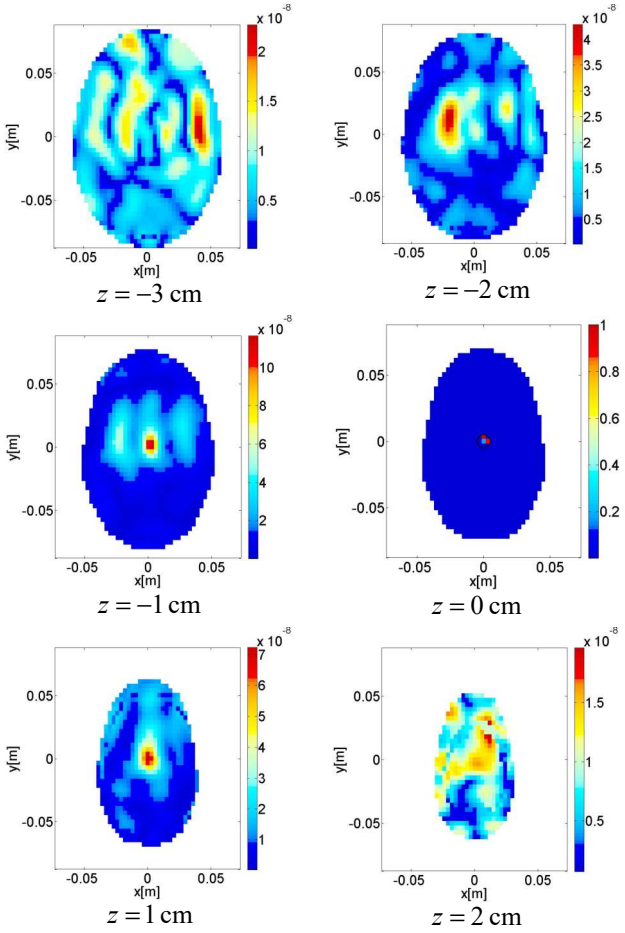

Figure 3. Reconstruction results obtained using the sparse microwave imaging algorithm. The radius of the stroke was $r = 0.5$ cm and $SNR = 10$ dB.

To study the resolution of the algorithm, we varied the stroke radius, r. Fig. 3 and Fig. 4 show the results in different planes obtained for $r = 0.5$ cm and $r = 1.5$ cm, respectively. The data were corrupted using the additive white Gaussian noise. The adopted signal to noise ratio was $SNR = 10$ dB, where the noise power was calculated with respect to the power of the differential scattering signal. As it could be seen from the images, the position of the stroke is clearly identified. (The cross-section of the stroke was denoted by the black line.)

5 Conclusion

We investigated the application of the sparse processing algorithm for estimating the stroke evolution between the measurements taken at different time instants. The algorithm was tested using the anthropomorphic human phantom designed for microwave medical imaging. We showed that the algorithm was capable of detecting targets of diameter as small as 1 cm in the case when a priori knowledge of the head tissue was available. As a future work, we will consider a more realistic scenario in which only limited information about the head is available.

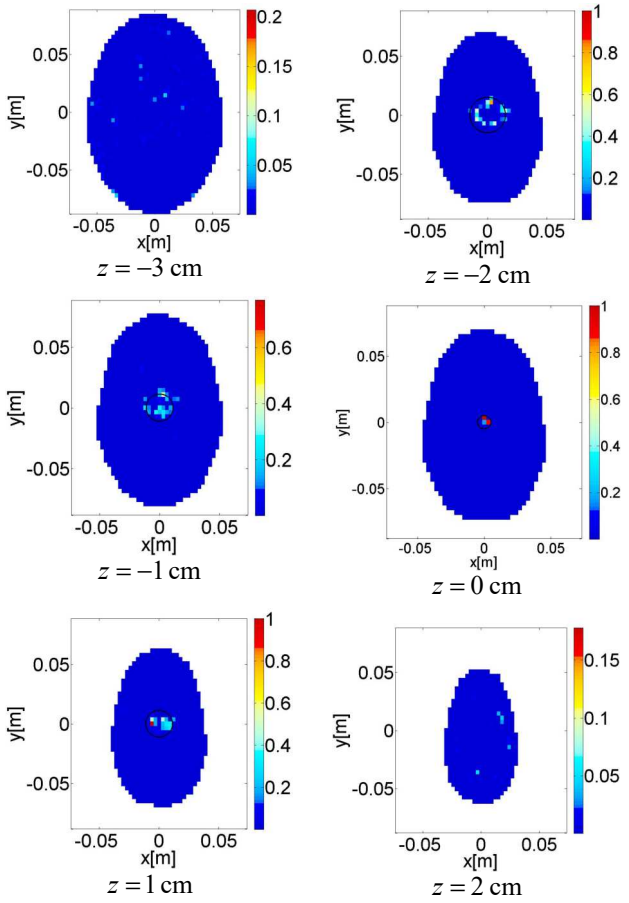

Figure 4. Reconstruction results obtained using the sparse microwave imaging algorithm. The radius of the stroke was $r = 1.5$ cm and $SNR = 10$ dB.

6 Acknowledgements

This work was supported by the EMERALD project funded from the European Union's Horizon 2020 research and innovation program under the Marie Skłodowska-Curie grant agreement No. 764479 and by the School of Electrical Engineering Belgrade, through the grant 1817/3 with the Ministry of Education, Science, and Technological Development of the Republic of Serbia.

7 References

1. L. Crocco, I. Karanasiou, M. James, R. Conceição, *Emerging Electromagnetic Technologies for Brain Diseases Diagnostics, Monitoring and Therapy*, Switzerland, Springer, 2016.

2. R. Conceição, J. Mohr, M. O'Halloran, *An Introduction to Microwave Imaging for Breast Cancer Detection, Switzerland*, Springer, 2018.

3. R. Scapaticci, L. D. Donato, I. Catapano, and L. Crocco, "A feasibility study on microwave imaging for

brain stroke monitoring," *Progress In Electromagnetics Research B*, vol. PIERB-40, pp. 305–324, 2012.

4. R. Scapaticci, O. M. Bucci, I. Catapano, and L. Crocco, "Differential microwave imaging for brain stroke followup," *Int. J. Antennas Propag*., Article ID 312528, 11 pages, 2014.

5. M. Persson et al., "Microwave-Based Stroke Diagnosis Making Global Prehospital Thrombolytic Treatment Possible," *IEEE Transactions on Biomedical Engineering*, vol. 61, no. 11, pp. 2806-2817, Nov. 2014.

6. J.A. Vasquez Tobon, R. Scapaticci, G. Turvani, G. Bellizzi, D. O. Rodriguez-Duarte, N. Joachimowicz, B. Duchêne, E. Tedeschi, M. R. Casu, L. Crocco, and F. Vipiana, "*A Prototype Microwave System for 3D Brain Stroke Imaging*," Sensors 2020, 20, 2607.

7. L. Crocco, L. Di Donato, I. Catapano, T. Isernia, "An improved simple method for imaging the shape of complex targets," *IEEE Transactions on Antenna and Propagation*, vol. 61, no. 2, pp. 843–851, 2013.

7. A. Massa, P. Rocca and G. Oliveri, "Compressive Sensing in Electromagnetics - A Review," *IEEE Antennas and Propagation Magazine*, vol. 57, no. 1, pp. 224–238, Feb. 2015.

8. M. Nikolic, A. Nehorai, and A. R. Djordjević, "Electromagnetic imaging of hidden 2D PEC targets using sparse signal modeling," *IEEE Transactions on Geoscience and Remote Sensing*, vol. 51, Issue: 5, Part: 1, pp. 2707–2721, May 2013.

9. M. Nikolic Stevanovic, L. Crocco, A. Djordjevic, and A. Nehorai, "Higher-order sparse microwave imaging of PEC scatterers," *IEEE Trans. Antennas Propag*., vol. 64, no. 3, pp. 988–997, 2016.

10. R. Solimene, F. Ahmad, and F. Soldovieri, "A novel CS-TSVD strategy to perform data reduction in linear inverse scattering problems," *IEEE Geosci. Remote Sens. Lett.*, vol. 9, no. 5, pp. 881–885, Sep. 2012.

11. M. Azghani, P. Kosmas, and F. Marvasti, "Microwave medical imaging based on sparsity and an iterative method with adaptive thresholding," *IEEE Transactions on Medical Imaging*, vol. 34, no. 2, pp. 357–365, 2015.

12. M. N. Stevanovic, R. Scapaticci and L. Crocco, "Three-dimensional sparse microwave imaging for brain stroke monitoring," *12th European Conference on Antennas and Propagation (EuCAP 2018)*, London, 2018, pp. 1-5.

13. E. Lagunas, M. G. Amin, F. Ahmad, and M. Najar, "Joint wall mitigation and compressive sensing for indoor image reconstruction," *IEEE Trans. Geosci. Remote Sens*., vol. 51, no. 2, pp. 891–906, Feb. 2013.

14. N. Joachimowicz, B. Duchêne, C. Conessa, O. Meyer, "Anthropomorphic Breast and Head Phantoms for Microwave Imaging," *Diagnostics*, 2018, 8(4) p85.

15. N. Nikolova, *Introduction to Microwave Imaging (EuMA High Frequency Technologies Series)*, Cambridge University Press, 2017.

16. WIPL-D Pro CAD 2019, WIPL-D d.o.o, Belgrade, 2019.

17. B. M. Kolundzija and A. R. Djordjevic, *Electromagnetic modeling of composite metallic and dielectric structures*, Boston, London, Artech House, 2002.